

Deriving temporally continuous soil moisture estimations at fine resolution by downscaling remotely sensed product

Yan Jin^{a,b}, Yong Ge^{a,b,*}, Jianghao Wang^{a,b,*}, Gerard B.M. Heuvelink^{c,d}

^a State Key Laboratory of Resources and Environmental Information Systems, Institute of Geographic Sciences & Natural Resources Research, Chinese Academy of Sciences, Beijing, 100101, China

^b University of Chinese Academy of Sciences, Beijing, 100049, China

^c Soil Geography and Landscape Group, Wageningen University, PO Box 47, 6700 AA, Wageningen, The Netherlands

^d ISRIC – World Soil Information, PO Box 353, 6700 AJ, Wageningen, The Netherlands

ARTICLE INFO

Keywords:

Downscaling
Temporal continuity
Geographically weighted regression
Soil moisture
AMSR-E
Tibetan plateau

ABSTRACT

Land surface soil moisture (SSM) has important roles in the energy balance of the land surface and in the water cycle. Downscaling of coarse-resolution SSM remote sensing products is an efficient way for producing fine-resolution data. However, the downscaling methods used most widely require full-coverage visible/infrared satellite data as ancillary information. These methods are restricted to cloud-free days, making them unsuitable for continuous monitoring. The purpose of this study is to overcome this limitation to obtain temporally continuous fine-resolution SSM estimations. The local spatial heterogeneities of SSM and multiscale ancillary variables were considered in the downscaling process both to solve the problem of the strong variability of SSM and to benefit from the fusion of ancillary information. The generation of continuous downscaled remote sensing data was achieved via two principal steps. For cloud-free days, a stepwise hybrid geostatistical downscaling approach, based on geographically weighted area-to-area regression kriging (GWATARK), was employed by combining multiscale ancillary variables with passive microwave remote sensing data. Then, the GWATARK-estimated SSM and China Soil Moisture Dataset from Microwave Data Assimilation SSM data were combined to estimate fine-resolution data for cloudy days. The developed methodology was validated by application to the 25-km resolution daily AMSR-E SSM product to produce continuous SSM estimations at 1-km resolution over the Tibetan Plateau. In comparison with ground-based observations, the downscaled estimations showed correlation ($R \geq 0.7$) for both ascending and descending overpasses. The analysis indicated the high potential of the proposed approach for producing a temporally continuous SSM product at fine spatial resolution.

1. Introduction

Land surface soil moisture (SSM) has vital importance in both the energy balance of the land surface and the water cycle (Seneviratne et al., 2010; Ochsner et al., 2013). A fine spatial resolution SSM dataset is one of the crucial input parameters for catchment-based hydro-ecological modeling (Li et al., 2015), drought and flood forecasting (Chakrabarti et al., 2014), weather and climate prediction (Koster et al., 2011), and crop growth monitoring (Tubiello et al., 2002). Ground-based measurement methods such as gravimetric measurements (Robock et al., 2000), electrical resistivity measurements (Samouëlian et al., 2005), and time domain reflectometry (Noborio, 2001) can yield accurate in situ soil moisture data at different depths. These techniques make the acquisition of simultaneous regional-scale measurements of

soil moisture feasible given the advent of wireless sensor networks (Jin et al., 2014; Ge et al., 2015) and the Cosmic-ray Soil Moisture Observing System (Zreda et al., 2012). However, the implementation of dense networks of instruments across large areas to obtain continuous SSM measurements is generally restricted because of financial and practical limitations. Furthermore, in situ measurements cannot characterize the large-scale variability attributable to the high spatial and temporal heterogeneities of SSM (Kang et al., 2017).

Remote sensing techniques are characterized by the advantages of large information capacity, huge observation scope, and high speed; thus, they have become the principal means of earth observation at regional, continental, and global scales. With the development of remote sensing techniques, satellite microwave observations acquired by active and passive sensors have increasingly been applied to retrieve

* Corresponding authors at: State Key Laboratory of Resources and Environmental Information Systems, Institute of Geographic Sciences & Natural Resources Research, Chinese Academy of Sciences, Beijing, 100101, China.

E-mail addresses: gey@lreis.ac.cn, gey@igsrr.ac.cn (Y. Ge), wangjh@lreis.ac.cn (J. Wang).

<https://doi.org/10.1016/j.jag.2018.01.010>

Received 12 December 2017; Received in revised form 20 January 2018; Accepted 26 January 2018

Available online 16 February 2018

0303-2434/ © 2018 Elsevier B.V. All rights reserved.

SSM via the physically based relationship between the soil dielectric constant and water content. Many satellite-based active and passive microwave sensors have been launched (Jackson et al., 2010; Jensen et al., 2011), including the Advanced Microwave Scanning Radiometer for the Earth Observing System (AMSR-E), Advanced Synthetic Aperture Radar (ASAR), Advanced Scatterometer, Soil Moisture and Ocean Salinity (SMOS), Advanced Microwave Scanning Radiometer 2 (AMSR-2), and Soil Moisture Active Passive (SMAP) instruments. Several related SSM products have also been made available, such as the AMSR-E Land Parameter Retrieval Model (Owe et al., 2008) and the SSM products from the Advanced Scatterometer (Naeimi et al., 2009), SMOS (Kerr et al., 2002), and SMAP (Entekhabi et al., 2010). Unfortunately, all of the above SSM products have coarse spatial resolution of the order of tens of kilometers. To monitor SSM at fine spatial resolution over large areas, the spatial resolution of existing SSM products must be downscaled (Atkinson, 2013; Malbêteau et al., 2017).

Various methods have been developed to downscale microwave-derived SSM products. These methods can be classified broadly into the following two categories based on the type of input data: a combination of active and passive microwave data (Wagner et al., 2008), and a combination of visible/infrared and microwave data. The change detection method (Njoku et al., 2002; Wagner et al., 2008), SMAP baseline algorithm (Das et al., 2011), and a Bayesian merging method (Zhan et al., 2006) have been proposed for merging radar (active) and radiometer (passive) data. However, because of the fine resolution of visible/infrared remote sensing data, it has become popular to combine them with coarse SSM remote sensing data in a downscaling procedure (Piles et al., 2011). General statistical methods (Wilson et al., 2005), machine learning methods (Ahmad et al., 2010; Srivastava et al., 2013), data assimilation (Sahoo et al., 2013a,b; Yang et al., 2016; Chen et al., 2017), universal triangle/trapezoidal models (Merlin et al., 2013, 2015), and geostatistical methods (Thattai and Islam, 2000; Chen et al., 2014) have been developed to obtain SSM by employing fine spatial resolution visible/infrared data. The idea behind these methods is to establish either statistical correlation or a physically based model between SSM and ancillary variables. A systematic review of the techniques for downscaling satellite remotely sensed SSM data and their potential for application was presented by Peng et al. (2017). However, some problems that remain in the downscaling process must be addressed, such as local heterogeneity, discontinuous downscaled estimations, and the enhancement of model representativeness.

Because SSM commonly has high spatial heterogeneity, global models might be inadequate in capturing its local variability. Strong surface heterogeneity would decrease the spatial correlation and increase the error in downscaled estimations. However, nonstationary models have been developed to deal with high spatial heterogeneity (Harris et al., 2010). For example, Jin et al. (2017) proposed the use of geographically weighted area-to-area regression kriging (GWATARK) to downscale the AMSR-2 SM product, which is a technique that integrates geographically weighted regression (GWR) and area-to-area kriging (ATAK).

Although the high accuracy of downscaled results has indicated the potential of combining visible/infrared data to estimate SSM at fine spatial resolution, one of the major limitations of the technique is the requirement for full-coverage visible/infrared data. However, the visible/infrared remotely sensed products generally cannot provide full coverage on a daily basis due to the cloud disturbance; thus, it is not possible to obtain continuous SSM estimations by employing visible/infrared data in downscaling procedures. Several reconstruction methods (Roy et al., 2008; Rakwatin et al., 2009; Chen et al., 2016) have been proposed to derive continuous satellite visible/infrared observations; however, limited research has been conducted on obtaining temporally continuous downscaling estimations (e.g., Sahoo et al., 2013a,b; Djamai et al., 2016). In addition to downscaling, some researchers (Zhao et al., 2013; Leng et al., 2014) focus on the SSM retrieval models to obtain continuous SSM estimations from the

combination of optical/infrared data and ancillary data (e.g. meteorological data, hydrologic data). In recent studies (Leng et al., 2016, 2017), a practical algorithm that uses the real temporal information of diurnal changes of satellite-derived land surface variables (e.g. LST, solar radiation) has been developed and applied in different biophysical and atmospheric conditions.

Most of the abovementioned methods assume the model between SSM and the ancillary variables is scale-invariant and they downscale SSM directly from the coarse-resolution dataset to the target fine resolution. The established downscaling model might not simulate the relationships at different resolutions effectively, and it might perform better under the condition of a smaller scale factor than a larger scale factor (e.g., from 25 to 1 km, the scale factor is 25). In addition to the ancillary variables at the coarse and target fine resolutions, data are also available at several intermediate resolutions that could provide further information to explain the SSM. For example, there are multiscale satellite products of both land surface temperature (LST) and normalized difference vegetation index (NDVI), which are two ancillary variables used often in SSM downscaling (Chauhan et al., 2003; Colliander et al., 2017), as well as multiscale soil texture information that could influence the pattern of SSM distribution (Reichle et al., 2010; Hengl et al., 2014). The use of multiscale ancillary information in the downscaling process is considered beneficial, and the stepwise method is an alternative approach with which to narrow the scale factor in each implementation of the downscaling and to make the best use of multiscale ancillary data.

To overcome the three weaknesses outlined above, this paper presents a methodology for the acquisition of continuous SSM at fine resolution, which considers local spatial heterogeneity of SSM, temporal discontinuity of SSM estimations, and multiscale ancillary information. This process is implemented via two principal steps. Because of its potential for addressing the local spatial heterogeneity problem, the GWATARK method is used on cloud-free days (Jin et al., 2017). Based on the GWATARK method, stepwise downscaling is implemented by combining multiscale ancillary variables with SSM. The coarse-resolution SSM data are downscaled through intermediate scales to the target fine resolution. On cloudy days, the GWATARK-estimated SSM and SSM data from another source are combined to estimate SSM at the target fine resolution. Then, the continuous downscaled estimations can be obtained. The proposed methodology was applied to improve the spatial resolution of the 25-km-resolution AMSR-E SSM product for both ascending and descending overpasses by integrating soil texture, LST, and NDVI information as ancillary variables. Fine-resolution (1 km) SSM estimations were acquired for the region of the Tibetan Plateau (TP), which includes two ground-based monitoring networks.

The structure of the rest of this paper is organized as follows. Section 2 describes both the study area and the data used. The downscaling methodology is described in Section 3. The downscaled results and their validation are presented in Section 4. Finally, several conclusions are drawn in Section 5.

2. Study area and data description

2.1. Study area

The study area comprised the TP in eastern Asia (26.5°–40.0°N, 73.4°–104.4°E), which is the highest plateau in the world (Zeng et al., 2015) (Fig. 1). It has average elevation of over 4000 m above sea level and it encompasses an area of approximately 2.5×10^6 km² (Qin et al., 2013). In order to both investigate the mechanism of soil–vegetation–atmosphere interactions and validate satellite SSM products, several soil moisture networks have been established on the TP (Su et al., 2011; Yang et al., 2013). These include two soil moisture and temperature measurement system (SMTMS) networks at Maqu and Naqu, which provide representations of different land surface conditions and climates. In the north-eastern fringe of the TP, the Maqu area is the largest

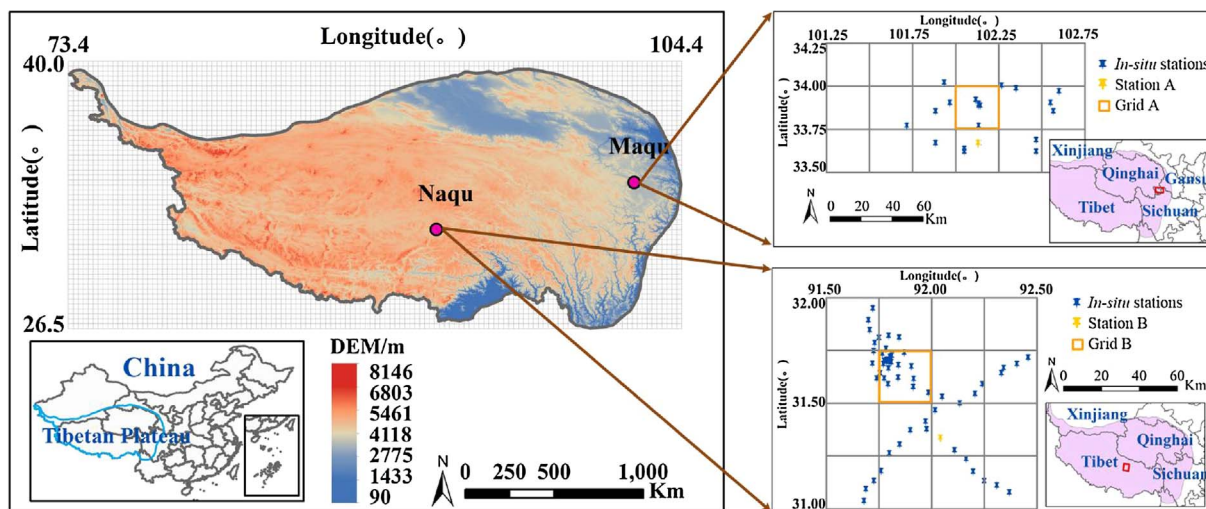


Fig. 1. Map of the Tibetan Plateau and the locations of the two SMTMS networks, including the distributions of the corresponding monitoring stations in each. Blue spots indicate in situ SSM stations. The two 25-km grids and the two ground stations shown in orange, identified as Grid A and Grid B, and as Station A and Station B, were used for analysis. (For interpretation of the references to colour in this figure legend, the reader is referred to the web version of this article.)

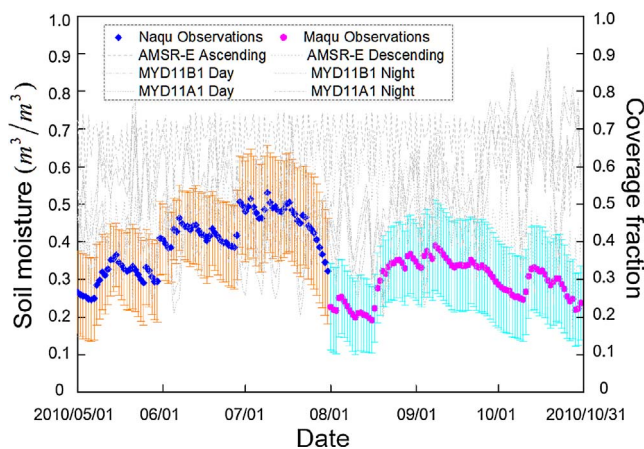


Fig. 2. Daily mean SSM observations and daily coverage fractions of remotely sensed products (i.e., MODIS and AMSR-E). Blue and purple dots represent mean values and the bars indicate ± 1 standard deviation. (For interpretation of the references to colour in this figure legend, the reader is referred to the web version of this article.)

wetland on the plateau and it is subject to high chilly an alpine and humid climate. Naqu lies within the subfrigid central part of the TP under the influence of the Asian summer monsoon; it has a subhumid climate with alpine meadow as the main vegetation type. The topography of the study area, locations of the ground-based SMTMS networks, and arrangement of the AMSR-E grid pixels are shown in Fig. 1. In the following analysis, the two AMSR-E grid pixels covering the highest numbers of ground-based sites and the two ground stations in the Maqu and Naqu areas are identified as Grid A and Grid B, and as Station A and Station B, respectively.

2.2. Soil observations

2.2.1. SMTMS networks

The SMTMS network of Maqu, established in July 2008 to monitor SSM and temperature, has acquired measurements from July 1, 2008 to July 31, 2010 (Su et al., 2011; Dente et al., 2012). The spatial distribution of the 20 ground stations that comprise the network is shown in Fig. 1. The International Soil Moisture Network (<http://ismn.geo.tuwien.ac.at/networks/maqu/>) provides dynamical SSM observations at depths of 5, 10, 20, 40, and 80 cm with temporal resolution of 15 min.

The SMTMS network of Naqu, comprising 56 ground stations, was established in July 2010 and designed for multiscale observation purposes (Fig. 1) (Yang et al., 2013). This multiscale network includes large- (1.0°), medium- (0.3°), and small-scale (0.1°) networks. The Data Assimilation and Modeling Center for Tibetan Multi-spheres (<http://dam.itpcas.ac.cn/>) has provided dynamical SSM observations at depths of 0–5, 10, 20, and 40 cm with temporal resolution of 30 min since August 1, 2010.

Because of the cold environment of the TP, soil thawing and freezing occur around May and November, respectively. For this study, six months' in situ SSM observations were collected from May 1 to October 31, 2010. The soil texture information (sand, clay, and silt contents) of the two SMTMS networks was also measured. The average surface observations during the three hours before and after satellite overpasses were collated to validate the SSM of the AMSR-E, i.e., from 22:30 to 04:30 local solar time for the descending overpasses and from 10:30 to 16:30 local solar time for the ascending overpasses. Two consecutive three-month periods were adopted for the validation in the Maqu and Naqu areas because of the availability of ground observations. The data comprised in situ SSM observations at 5-cm depth from the Maqu area (from May 1 to July 31, 2010) and at depths of 0–5 cm from the Naqu area (from August 1 to October 31, 2010). Fig. 2 shows the daily mean and standard deviation values of SSM during the entire six-month period, together with the daily coverage fraction of the remote sensed products.

2.2.2. AMSR-E data

The AMSR-E instrument was launched on May 4, 2002, to acquire global observations of SSM (Njoku et al., 2003), and to ascertain the feasibility for downscaling SSM products (Ray et al., 2010). Daily AMSR-E (version 002) level 3 products at 25-km spatial resolution, derived from descending (01:30 local solar time) and ascending (13:30 local solar time) overpasses, were retrieved using the Land Parameter Retrieval Model based on the X band (<https://earthdata.nasa.gov/>). Full-coverage data were chosen from six months as valid data. These were then resampled into 25×25 km regular grids (Fig. 1) using the nearest neighbor resampling technique to provide complete coverage of the study area.

2.2.3. SSM assimilation datasets

The China Soil Moisture Dataset from Microwave Data Assimilation (CSMDA) data were employed to estimate fine-scale SSM on cloudy days through combination with the downscaled results obtained on

cloud-free days. The SSM assimilation datasets were estimated using a Dual-Pass Microwave Land Data Assimilation System at the Data Assimilation and Modeling Center (Yang et al., 2007) and subsequently validated (Yang et al., 2016). These temporally continuous datasets comprise daily SSM data at 25-km spatial resolution at three layers (0–5, 5–20, and 20–100 cm) from June 20, 2002 to September 24, 2011, which are free to download (<http://en.tpdatabase.cn/portal/index.jsp>). The six-month SSM assimilation data at depths of 0–5 cm from the studied areas of the TP were resampled to the same grid configuration as the AMSR-E data.

2.2.4. Gridded soil data

Gridded soil data were selected as ancillary variables in the SSM downscaling because of their influence on the pattern of distribution of SSM. The International Soil Moisture Network (<http://www.isric.org/>) has released two versions of the Global Soil Information system (SoilGrids) for the estimation of detailed soil properties (Hengl et al., 2014, 2017). These two soil profile datasets include information at six different depths (2.5, 10.0, 22.5, 45.0, 80.0, and 150.0 cm) with spatial resolutions of 1 km (first version) and 250 m (second version). Given that our concern was soil surface information, soil texture data (clay, sand, and silt contents) at 2.5-cm depth from the first version of the dataset were used. The soil texture data covering the study area were resampled to 1-km resolution using the nearest neighbor resampling technique, and then aggregated to 5 and 25 km bins using the average aggregating technique.

2.3. MODIS products

The LST and NDVI were also chosen as ancillary variables for the SSM downscaling. Given that the equator crossing times of a sun-synchronous satellite are 01:30 and 13:30 local solar time, the MODIS data available for this study included four MODIS products (version 006) of the Aqua satellite: 1-km daily LST (MYD11A1), 6-km daily LST (MYD11B1), 1-km 16-day NDVI (MYD13A2), and 0.05° 16-day NDVI (MYD13C1). These products are available for download from the NASA Land Data Products and Services website (<https://search.earthdata.nasa.gov/search>). The day and night LSTs were extracted from the MYD11A1 and MYD11B1 products, corresponding to the ascending and descending overpasses, respectively. The two 16-day NDVI products are cloud free. To avoid the influence of cloud, coincident dates with high fractions of data coverage (> 0.5) were selected from the two LST products as cloud-free days using the spline interpolation technique for interpolating uncovered pixels. After matching the AMSR-E and MODIS data, 52 days of ascending overpasses and 47 days of descending overpasses were selected as the full-coverage days. Fig. 3 displays these valid days during the six-month period, illustrating the obvious discontinuity. All MODIS data were projected and extracted consistently

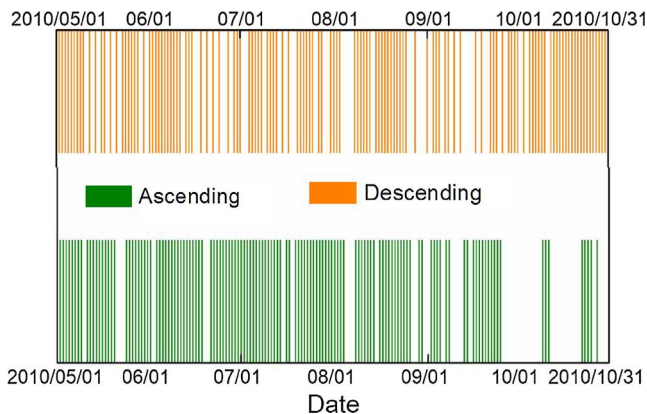


Fig. 3. Days of valid remote sensing data during the six-month period for ascending and descending overpasses.

with large-scale AMSR-E data. The data of MYD11A1 and MYD13A2 were resampled to 1-km resolution. The data of MYD11B1 and MYD13C1 were resampled to 5-km resolution and then aggregated to 25-km bins.

2.4. DEM products

The NASA Shuttle Radar Topographic Mission (Jarvis et al., 2008) provides digital elevation model (DEM) data at 30- and 90-m spatial resolutions, which are available to download (<http://srtm.csi.cgiar.org/>). This study used the version 4 DEM product at 90-m spatial resolution, which was resampled to 1×1 km regular grids by averaging the values of all the pixels within each 1-km pixel.

3. Methodology

To address the problems of local heterogeneity, discontinuous downscaled estimations, and the enhancement of model representativeness in the downscaling process, this paper describes a strategy for obtaining continuous downscaled SSM estimations at fine resolution. A flowchart of the proposed downscaling strategy, for which all data should be preprocessed, is presented in Fig. 4. The strategy comprises two principal aspects for the estimation of SSM at 1-km resolution: a) stepwise downscaling on full-coverage days using GWATARK, and b) downscaling on cloudy days through modeling the function between GWATARK-estimated SSM (obtained in step a) and CSMDA data. Further details are provided in the following.

3.1. Stepwise downscaling on full-coverage days

The GWATARK method is used repeatedly for stepwise downscaling on full-coverage days to downscale SSM from a coarse resolution (25 km) to a finer resolution (1 km) through an intermediate scale (5 km). Assume that nF^2 spatially distributed pixels G_o^{fine} ($o = 1, 2, \dots, nF^2$) and n pixels G_o^{coarse} ($O = 1, 2, \dots, n$) are the fine- and coarse-resolution pixels, respectively, where F is the scale factor. Let $Z_1(\cdot)$ denote the SSM observations on full-coverage days. Thus, the GWATARK estimation is

$$\hat{Z}_1(G_o^{\text{fine}}) = \hat{m}(G_o^{\text{fine}}) + \hat{R}(G_o^{\text{fine}}), \quad (1)$$

where $\hat{m}(G_o^{\text{fine}})$ and $\hat{R}(G_o^{\text{fine}})$ are the trend component and the residual component at fine resolution, respectively. The GWATARK is a hybrid method that comprises GWR for spatial trends and ATAK for downscaling regression residuals. For details, the reader is referred to Jin et al. (2017).

The SSM predictions at 1-km spatial resolution can be obtained by repeated use of Eq. (1). A two-step downscaling process was employed because of the available two-scale ancillary information. The scale factor in each implementation of the downscaling would narrow to 5 from 25. The GWATARK is implemented twice in this paper, downscaling SSM from 25 km to 5 km and then to 1 km. Let G_i^l be pixel G_i at l ($l = 0$ for 25 km, 1 for 5 km, and 2 for 1 km) resolution, where $i = 1, 2, \dots, \text{num}$. The parameter num is different for each scale and it represents the total number of observation pixels at the current spatial resolution. For convenience, we define that pixel G_i^2 is located within pixel G_i^1 and that pixel G_i^1 is located within pixel G_i^0 . As mentioned in Introduction section, LST, NDVI and soil texture are related to SSM. In this paper, four ancillary variables, i.e., sand, clay, LST, and NDVI, are employed as the covariates in SSM downscaling. Only two of the three SSM texture parameters were chosen because the silt content can be represented by a combination of the sand and clay contents. For spatial trends, the relationship between the SSM and four covariates at fine resolution is modeled by linear regression by using the GWR model. And ATAK is employed to downscale the regression residuals to obtain predictions of the residuals at fine resolution. Let $x(\cdot)$ denote the covariates. First, we set $l = 1$, meaning that the AMSR-E SSM 25-km-resolution data are

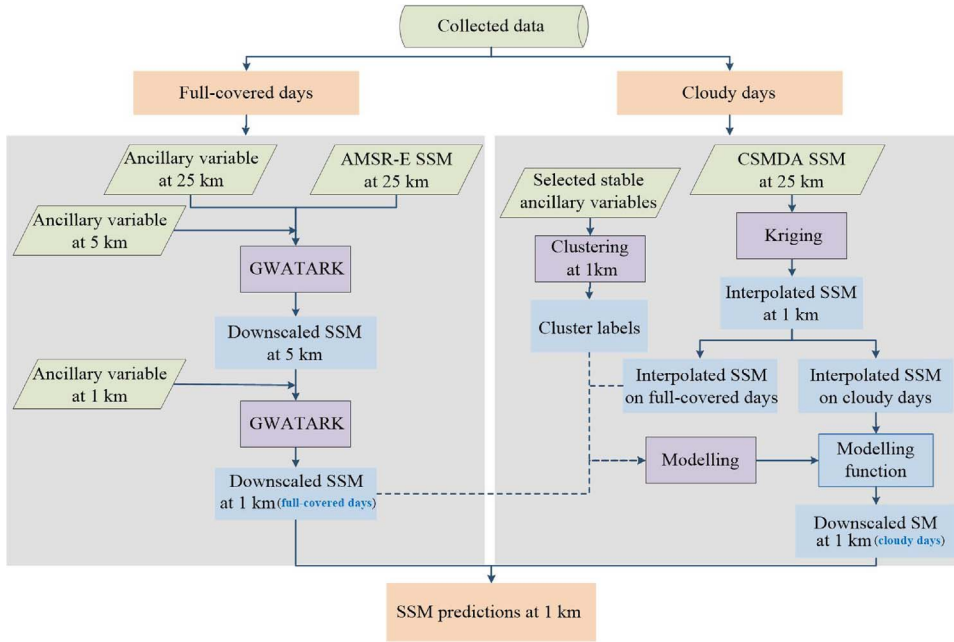


Fig. 4. Flowchart of the proposed downscaling methodology.

downscaled to 5-km resolution, which can be written as:

$$\begin{aligned} \hat{Z}_1(G_i^1) = \hat{m}(G_i^1) + \hat{R}(G_i^1) = & \hat{\beta}_0(G_i^0) + \hat{\beta}_{\text{Sand}}(G_i^0) \cdot x_{\text{Sand}}(G_i^1) + \hat{\beta}_{\text{Clay}}(G_i^0) \\ & \cdot x_{\text{Clay}}(G_i^1) + \hat{\beta}_{\text{LST}}(G_i^0) \cdot x_{\text{LST}}(G_i^1) + \hat{\beta}_{\text{NDVI}}(G_i^0) \cdot x_{\text{NDVI}}(G_i^1) \\ & + \sum_{h=1}^M \lambda_{hi}^0 \cdot \left\{ Z_1(G_h^0) - [\hat{\beta}_0(G_h^0) + \hat{\beta}_{\text{Sand}}(G_h^0) \cdot x_{\text{Sand}}(G_h^0) + \hat{\beta}_{\text{Clay}}(G_h^0) \right. \\ & \left. \cdot x_{\text{Clay}}(G_h^0) + \hat{\beta}_{\text{LST}}(G_h^0) \cdot x_{\text{LST}}(G_h^0) + \hat{\beta}_{\text{NDVI}}(G_h^0) \cdot x_{\text{NDVI}}(G_h^0)] \right\}. \end{aligned} \quad (2)$$

Then, we set $l = 2$, meaning the above SSM estimations at 5-km resolution are downscaled to 1-km resolution (Eq. (3)), where $\hat{Z}_1(G_i^2)$ is the estimated SSM value of pixel G_i at 1-km spatial resolution:

$$\begin{aligned} \hat{Z}_1(G_i^2) = \hat{m}(G_i^2) + \hat{R}(G_i^2) = & \hat{\beta}_0(G_i^1) + \hat{\beta}_{\text{Sand}}(G_i^1) \cdot x_{\text{Sand}}(G_i^2) + \hat{\beta}_{\text{Clay}}(G_i^1) \\ & \cdot x_{\text{Clay}}(G_i^2) + \hat{\beta}_{\text{LST}}(G_i^1) \cdot x_{\text{LST}}(G_i^2) + \hat{\beta}_{\text{NDVI}}(G_i^1) \cdot x_{\text{NDVI}}(G_i^2) \\ & + \sum_{h=1}^M \lambda_{hi}^1 \cdot \left\{ Z_1(G_h^1) - [\hat{\beta}_0(G_h^1) + \hat{\beta}_{\text{Sand}}(G_h^1) \right. \\ & \cdot x_{\text{Sand}}(G_h^1) + \hat{\beta}_{\text{Clay}}(G_h^1) \cdot x_{\text{Clay}}(G_h^1) + \hat{\beta}_{\text{LST}}(G_h^1) \\ & \left. \cdot x_{\text{LST}}(G_h^1) + \hat{\beta}_{\text{NDVI}}(G_h^1) \cdot x_{\text{NDVI}}(G_h^1)] \right\} \end{aligned} \quad (3)$$

3.2. Downscaling on cloudy days

As mentioned above, the stepwise downscaling process based on GWATARK is limited by its requirement for full-coverage input data. On cloudy days, the CSMDA data were incorporated to address this problem. First, the collected CSMDA SSM data are interpolated spatially using a kriging method (Cressie, 1988) to obtain 1-km-resolution SSM data for the period of interest, which includes both full-coverage and cloudy days:

$$\hat{Z}_2(G_i^2) = \sum_{e=1}^K \lambda_e \hat{Z}_2(G_e^0) \quad (4)$$

where λ_e represents the weights and K indicates how many coarse neighboring pixels are used to estimate the given fine-resolution pixels

in ordinary kriging.

Second, some stable ancillary information correlated to SM is used to perform clustering of the fine pixels. Here, the DEM and the sand and clay contents are selected as cluster variables, and the K -means technique (Likas et al., 2003), which is a common clustering method, is used to identify different regions of similarity within the 1-km gridded pixels. The recurrence of K -means technique would be implemented with various clustering numbers. Then, for each result of clustering, the correlations between 1-km CSMDA-derived and GWATARK-estimated SSM data could be calculated at corresponding clusters. In this experiment, the clustering number is set to 50 because the mean of the correlations reaches the highest value, with varying the clustering number from 20 to 100 at an interval of 10. By comparing the 1-km CSMDA-derived SSM data with the GWATARK-estimated SSM data (see Section 3.1), a relationship for each cluster between the two datasets can be derived:

$$Z_1^d = a_d + b_d \cdot Z_2^d, \quad (5)$$

where a_d and b_d are regression parameters, and Z_1^d and Z_2^d are 1-km SSM data on the same day for the d^{th} cluster estimated from the AMSR-E and CSMDA SSM data, respectively.

Based on the effectiveness of the established relationships for full-coverage days, the relationships in Eq. (5) can be applied for all days. Thus, the 1-km CSMDA-derived SSM data can be used as input data to acquire the corresponding 1-km-resolution estimates of SSM. At this point, temporally continuous SSM estimations at 1-km resolution can be obtained for the period of interest.

Given that ground-based measurements can provide high-quality SSM information that could increase estimation accuracy (Kaheil et al., 2008), the AMSR-E SSM products should be calibrated using ground-based measurements as a first step. This is independent of the downscaling process and it could reduce systematic errors in the downscaled results (Merlin et al., 2013). Support vector regression (SVR) (Vapnik, 2000; Ahmad et al., 2010) could be used to model the relationships between the AMSR-E data and the in situ observations of the two SMTMS networks. Fitted SVR models for the two three-month periods of this study can only be applied to regions that have conditions similar to the corresponding ground-based measurements. The value ranges of conditional information relating to the ground stations in the different SMTMS networks could be considered as restrictive elevations of 3634.5 ± 201.5 m and 4732.5 ± 144.5 m, sand contents of

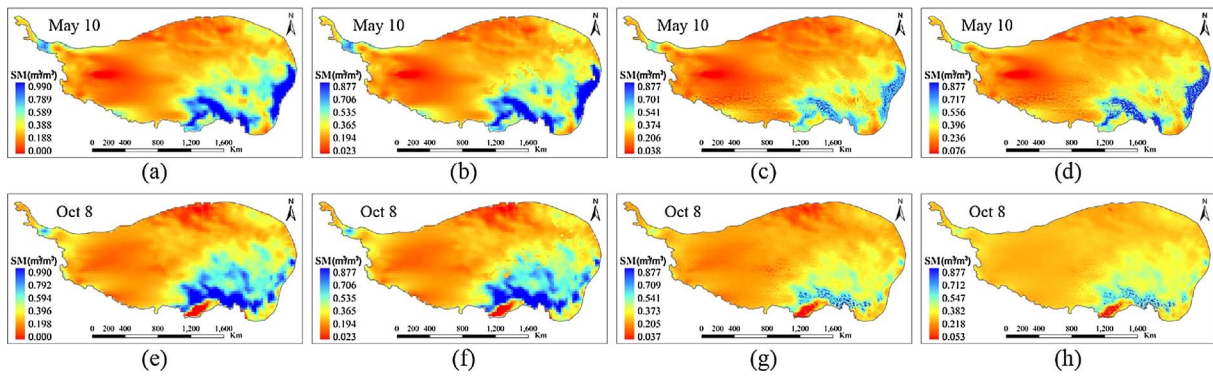


Fig. 5. SSM from ascending overpasses on two cloud-free days (i.e., May 10 and October 8, 2010): (a) and (e) 25-km original AMSR-E image, (b) and (f) 25-km SSM image, (c) and (g) downscaled 5-km SSM image, and (d) and (h) downscaled 1-km SSM image.

0.4111 ± 0.0554 and 0.4849 ± 0.0175 , and clay contents of 0.2014 ± 0.0302 and 0.1918 ± 0.0143 for the first (corresponding to Maqu stations) and second (corresponding to Naqu stations) three-month periods, respectively.

4. Results and discussion

The proposed methodology outlined above was applied using the 25-km-resolution daily AMSR-E SSM product over the TP for a six-month period (from May 2010 to October 2010). For its validation, several statistical parameters were computed between the 1-km SSM estimations and the corresponding in situ data, i.e., the root mean square error (*RMSE*) ($\text{m}^3 \text{m}^{-3}$), mean error (*ME*) ($\text{m}^3 \text{m}^{-3}$), correlation coefficient (*R*), and slope (*S*). The methodology described in this paper was implemented using the R language for statistical computing (Team, 2014).

4.1. AMSR-E SSM downscaling on cloud-free days

Figs. 5 and 6 display the 25-km AMSR-E SSM images and 1-km SSM estimations on two cloud-free days for ascending and descending cases. The spatial variations of the downscaled SSM are similar, i.e., SSM generally decreases from the southeast toward the northwest over the entire study area, but with an increase in the northwest corner. The estimated SSM images display close correlation with the spatial distribution of vegetation; areas of higher vegetation coverage show higher SM, and vice versa.

Fig. 7 compares the 1-km SSM estimations with in situ measurements. For both overpasses, the scatter plots (where one point represents one day) generally follow the 1:1 line, especially for the ascending overpasses. The statistical indices also indicate good agreement between the ground-measured and downscaled SSM data over the two

networks for the ascending overpasses, with an *RMSE* value of $0.127 \text{ m}^3 \text{ m}^{-3}$, *ME* value of $-0.046 \text{ m}^3 \text{ m}^{-3}$, *R* value of 0.737, and *S* value of 0.786. Furthermore, the *RMSE* value of $0.137 \text{ m}^3 \text{ m}^{-3}$, *ME* value of $-0.054 \text{ m}^3 \text{ m}^{-3}$, *R* value of 0.685, and *S* value of 0.623 indicate the same conclusion for the descending overpasses.

The *R* values for both overpass cases are < 0.75 . This could reflect the loss of some information when considering only four ancillary variables (i.e., LST, NDVI, and sand and clay contents) in the GWATARK-estimation method. The incorporation of other ancillary variables such as soil temperature and evapotranspiration could provide useful complementary information on SSM. If the ancillary variables are available at several different resolutions, the stepwise method would make use of multiscale ancillary information to explain the SSM and narrow the scale factor in each implementation of the downscaling. The GWATARK used in two-step downscaling could improve the ability of proposed downscaling strategy to effectively settle the local spatial heterogeneity and the change of support problem. Furthermore, the stepwise downscaling method need not be limited to just two steps; additional intermediate scales could be employed easily in the proposed strategy. The applicability of the downscaling model might be ambiguous when the scale factor is large, stepwise downscaling is able to avoid this problem. In this paper, the scale factor is reduced from 25 (directly downscaling from 25 km to 1 km) to 5. Although multiple covariates and multiscale data could contribute useful information, they would also introduce some errors, causing by the errors of input data and multiscale models. For instance, additional uncertainty would result from the use of a greater number of intermediate scales, which would need to be balanced against the accuracy of the derived estimations. Moreover, the relationships between SSM and the ancillary variables were assumed scale-invariant for SSM stepwise downscaling at the coarse and fine scales. In future research, scale effects on the SSM downscaling process should be investigated.

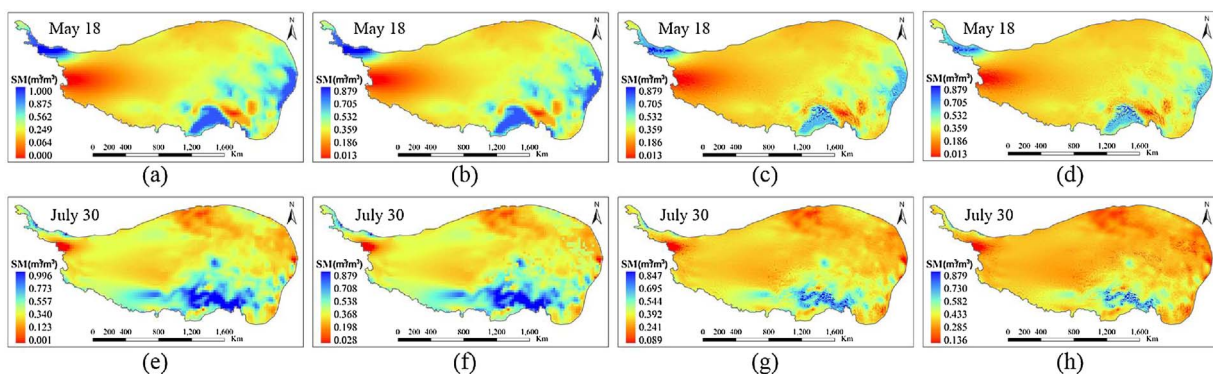


Fig. 6. SSM from descending overpasses on two cloud-free days (i.e., May 18 and July 30, 2010): (a) and (e) 25-km original AMSR-E image, (b) and (f) 25-km SSM image, (c) and (g) downscaled 5-km SSM image, and (d) and (h) downscaled 1-km SSM image.

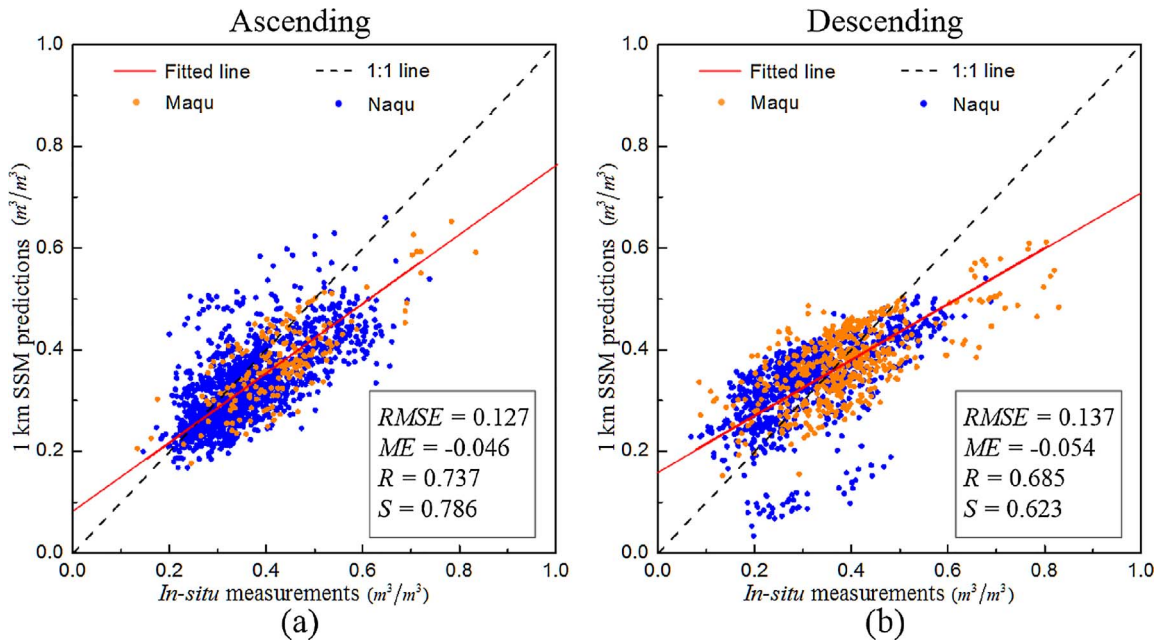


Fig. 7. 1-km SSM estimations versus in situ SSM, together with a summary of the comparison results on cloud-free days: (a) ascending overpasses and (b) descending overpasses.

4.2. SSM estimations at fine resolution on cloudy days

Because of the requirement for full-coverage visible/infrared input data, the GWATARK stepwise downscaling method cannot be applied on cloudy days. The CSMDA data were combined to estimate fine-resolution data for cloudy days. The means of correlations between original AMSR-E data and CSMDA data on each of full-cover days for ascending and descending overpasses are larger than 0.5 (Fig. 8(a)). As described in Section 3.2, on cloudy days, fine-resolution SSM is obtained by combining 1-km GWATARK-estimations (see Section 4.1) with 1-km CSMDA-derived SSM data (Eq. (5)). Instead of using CSMDA-derived SSM, a land surface model could be used to provide 1-km SSM. However, it must be noted that the forcing data used in a land surface model, including atmospheric and environmental geophysical data, must also satisfy the requirement for full-coverage, which could be achieved using reconstruction techniques.

Fig. 8(b) shows substantial discrepancy between the 1-km CSMDA-derived SSM data and the daily averaged in situ observations during the six-month study period, with a large RMSE value of $0.161 \text{ m}^3 \text{ m}^{-3}$, large ME value of $0.114 \text{ m}^3 \text{ m}^{-3}$, low S value of 0.172, and small R value of 0.345. The errors associated with the kriging method (Eq. (4)) might contribute most to such discrepancy because ordinary kriging ignores the change-of-support problem in the estimation process. The established models for cloud-free days between the GWATARK-estimated SSM and the 1-km CSMDA-derived SSM data were trained for each cluster. Then, they were used to generate the 1-km SSM estimations for cloudy days, which could reduce model errors under different conditions and improve the SSM estimation accuracy. In this experiment, the DEM and soil texture stable variables were chosen as clustering factors. In future, alternative references to distinguish conditions could include surface slope, land cover classification, and other factors.

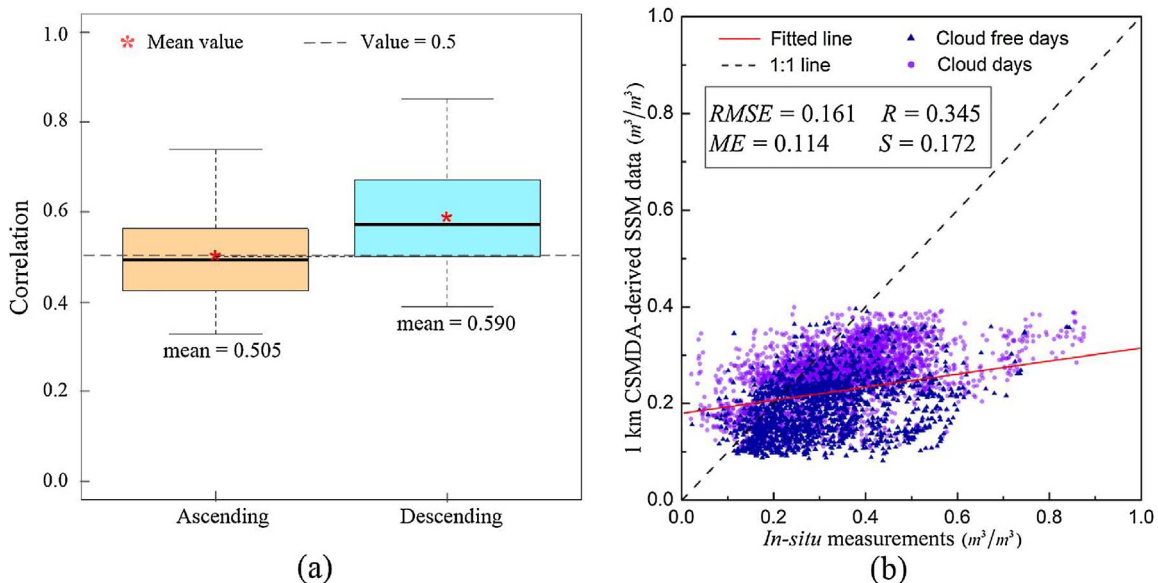


Fig. 8. (a) Boxplot of correlations between original AMSR-E data and CSMDA data on each of full-cover days for both overpasses and (b) 1-km CSMDA-derived SSM data versus in situ SSM on all days.

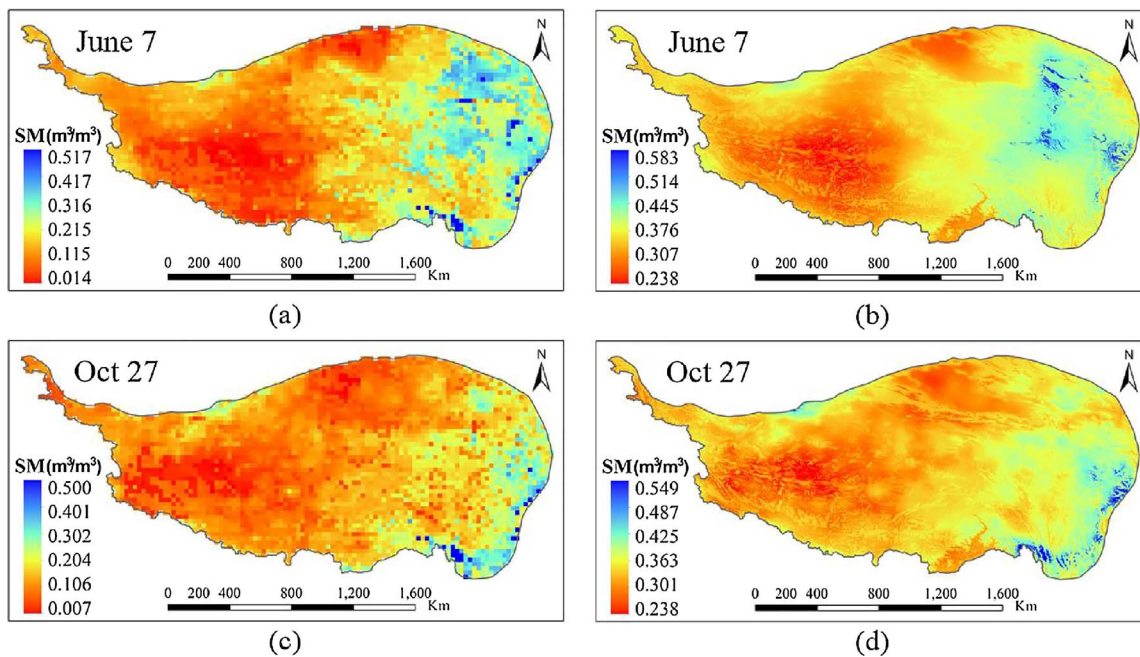


Fig. 9. SSM from ascending overpasses on two cloudy days (i.e., June 7 and October 27, 2010): (a) and (c) 25-km CSMMA image, and (b) and (d) corresponding 1-km SSM estimations.

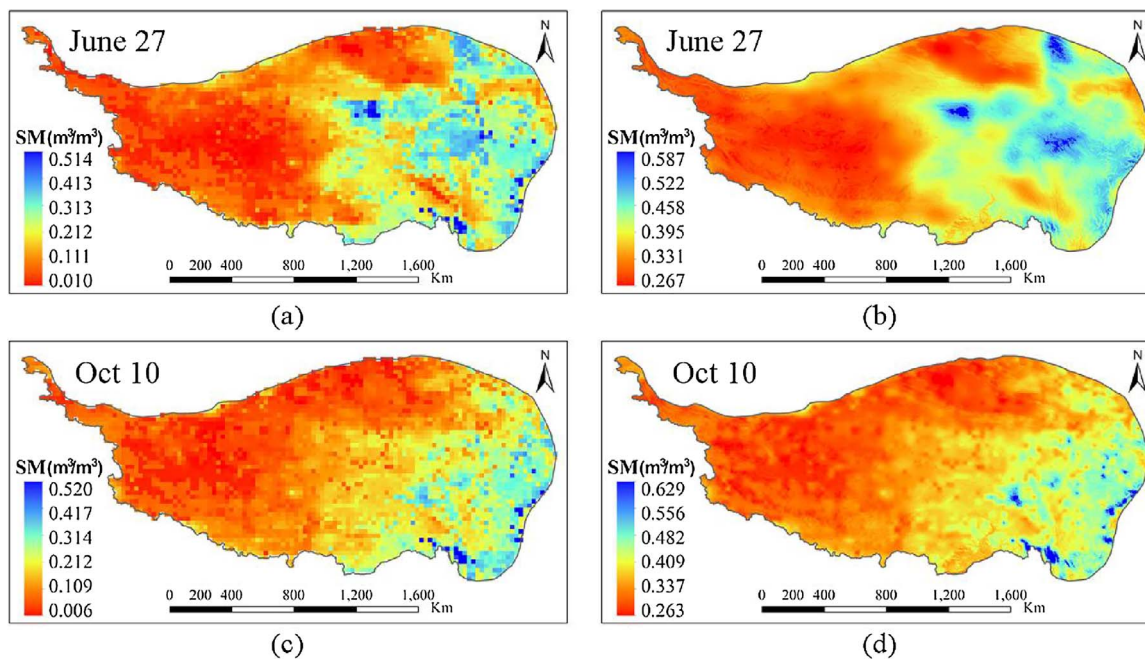


Fig. 10. SSM from descending overpasses on two cloudy days (i.e., June 27 and October 10, 2010): (a) and (c) 25-km CSMMA image, and (b) and (d) corresponding 1-km SSM estimations.

Figs. 9 and 10 show 25-km CSMMA images and 1-km SSM estimations for two cloudy days for ascending and descending overpasses, respectively. The blue areas in the images represent the largest SSM values. Similar to the trends of the downscaled images shown in Figs. 5 and 6, the spatial variations of the 1-km SSM show a general decrease from the southeast toward the northwest. The downscaled SSM estimations present greater spatial detail when compared with the coarse images. The scatter plots of the 1-km SSM estimations and the ground-based measurements on cloudy days for the ascending and descending overpasses are illustrated in Fig. 11. The values of $RMSE$, ME , R , and S are $0.138 \text{ m}^3 \text{ m}^{-3}$, $-0.056 \text{ m}^3 \text{ m}^{-3}$, 0.868 , and 0.556 , respectively, for the ascending overpasses, and $0.151 \text{ m}^3 \text{ m}^{-3}$, $-0.086 \text{ m}^3 \text{ m}^{-3}$, 0.759 , and 0.504 for the descending overpasses. These statistical indices indicate that the 1-km SSM estimations agree well with the ground-based

observations. In this experiment, the simple linear regression models were applied to fill the gap of SSM estimations on cloudy days, benefiting from its simple, tending to realize and few parameters. However, the dynamic variation rules of SSM were ignored by using such general statistical techniques. In future research, the SSM temporal information would be involved and make a contribution to accurate estimations.

4.3. Temporally continuous series of fine-resolution SSM

To investigate further the performance of the downscaling methodology, time series comparisons were undertaken on two stations and two 25-km grids. The temporal profiles of in situ SSM measurements obtained at Stations A and B, and the corresponding downscaled 1-km SSM estimations from Grids A and B, in the Maqu and Naqu regions,

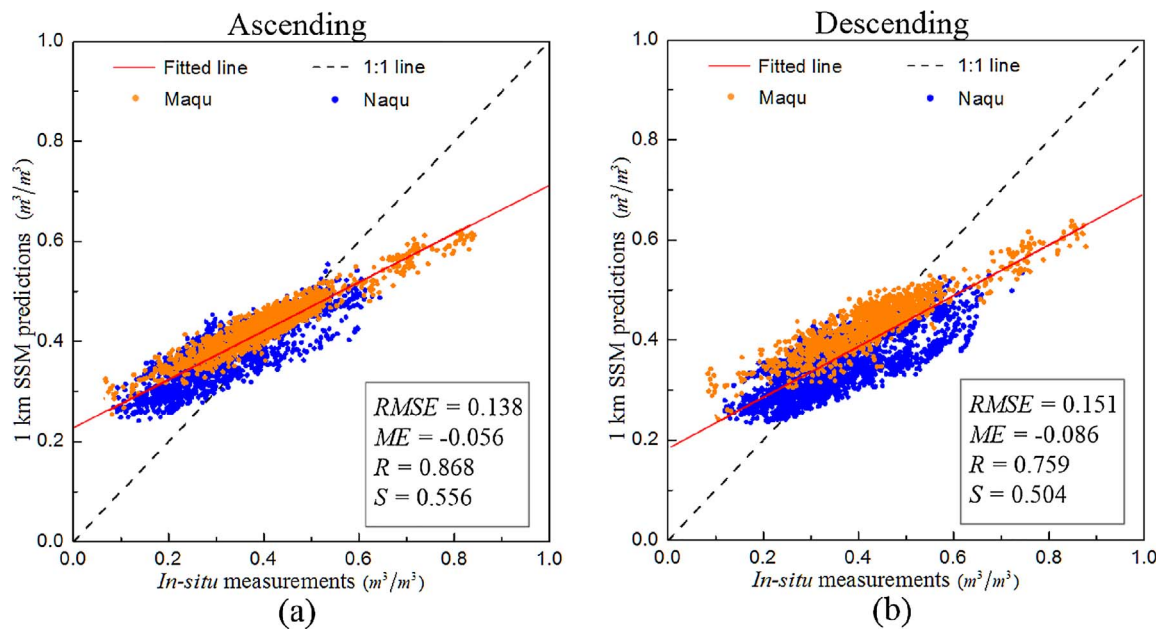


Fig. 11. 1-km SSM estimations versus in situ SSM, together with a summary of the comparison results on cloudy days: (a) ascending overpasses and (b) descending overpasses.

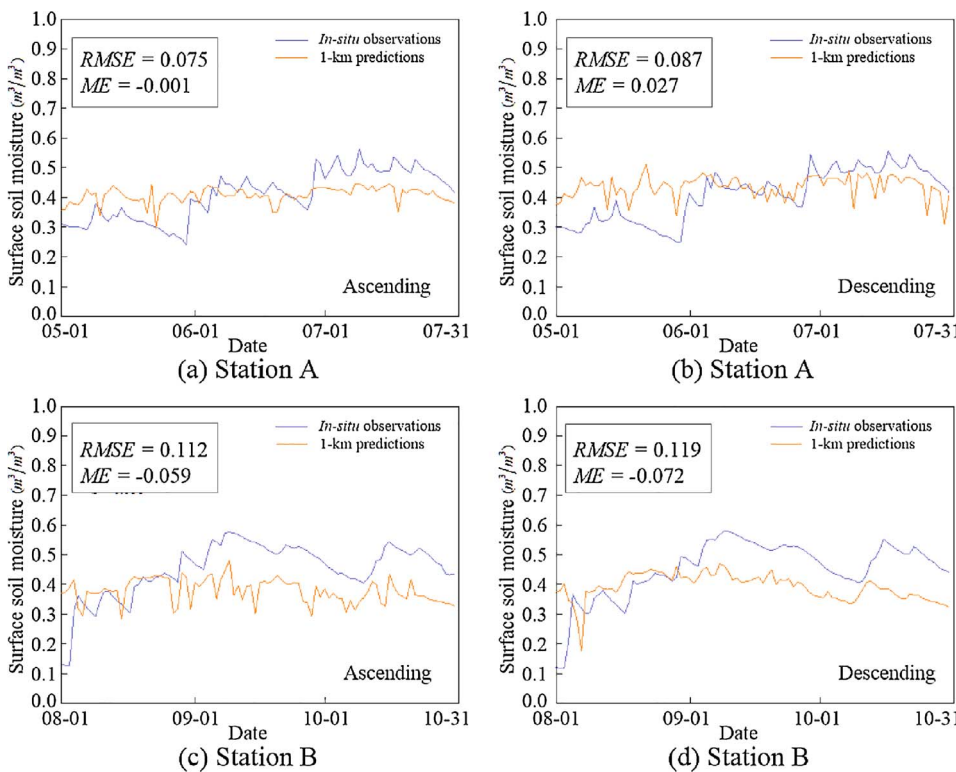


Fig. 12. Temporal profiles of SSM measurements at the ground stations and the corresponding downscaled 1-km SSM estimations. Three months' data (from May 2010 to July 2010) at Station A within the Maqu region: (a) ascending overpasses and (b) descending overpasses, and three months' data (from August 2010 to October 2010) at Station B within the Naqu region: (c) ascending overpasses and (d) descending overpasses.

respectively, are presented in Fig. 12. For both overpasses, the time series of downscaled SSM estimations show trends similar to the ground-based measurements. In addition, Fig. 13 shows comparisons of the temporal profiles of the downscaled 1-km SSM estimations, in situ SSM measurements, and original 25-km SSM data in Grids A and B for ascending and descending overpasses, together with the RMSE and R statistical indices. The presented temporal profiles contain the aggregated averages of the 1-km SSM estimations and in situ SSM measurements within Grids A and B, and the corresponding 25-km SSM data from AMSR-E and CSMDA. The RMSE and ME values for each Grid for both overpasses are reduced when compared with the original 25-km SSM data. The aggregated averages of in situ SSM measurements

might be inadequate for capturing the gridded SSM values because of the small number of ground stations within each grid.

As illustrated in the time series comparisons, the four temporal profiles for Stations A and B and for Grids A and B represent the seasonal variations well, with large SSM values from June to September. Although comparison at the same spatial resolution could overcome the representativeness errors to some extent, the complicated uncertainties in the aggregation processes should be considered further. In general, satisfactory performance of the proposed downscaling methodology could be concluded.

For all days, the discrete distributions of downscaled 1-km SSM estimations for the different overpasses and cases are illustrated in

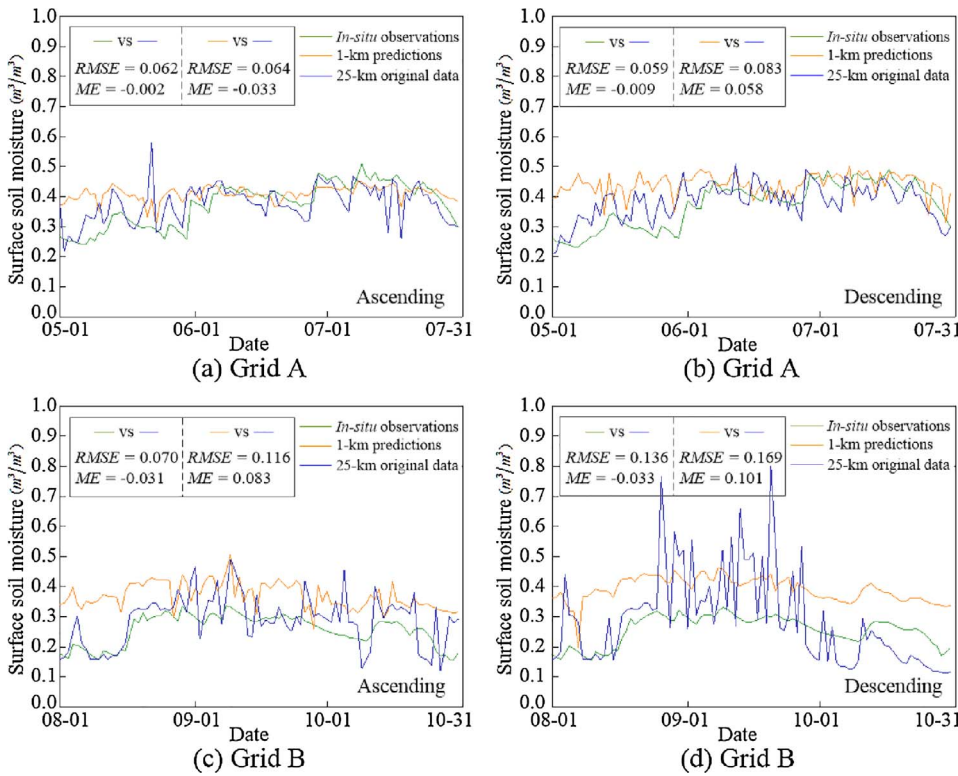


Fig. 13. Temporal profiles of in situ SSM measurements, downscaled 1-km SSM estimations, and original 25-km SSM data in Grids A and B. Three months' data (from May 2010 to July 2010) in Grid A within the Maqu region: (a) ascending overpasses and (b) descending overpasses, three months' data (from August 2010 to October 2010) in Grid B within the Naqu region: (c) ascending overpasses and (d) descending overpasses.

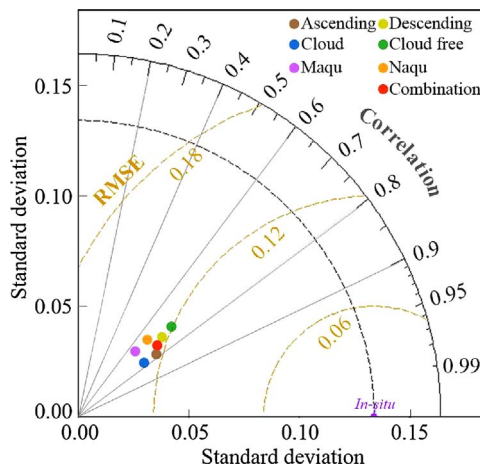


Fig. 14. Sample Taylor diagram displaying statistical comparisons between 1-km SSM downscaled estimations and in situ SSM measurements during the six-month study period for both overpasses.

Fig. 14 using a sample Taylor diagram in terms of three statistics: R , the standard deviation, and $RMSE$. The downscaled comparison results showed good correlation ($R \geq 0.7$) for both overpasses, although the results for the ascending overpasses had better performance, as indicated by the lower $RMSE$ value of $0.133 \text{ m}^3 \text{ m}^{-3}$. This might be related to additional errors in the AMSR-E descending product or, conversely, to the benefit derived from the stable LST in the AMSR-E ascending product. The differences between the downscaled results and the ground-based observations are attributable not only to the prediction errors of the models and to the measurement errors of the original SSM observations and multiscale covariates, but also to the representativeness errors of the point and 1-km gridded SSM data. The errors of input data would propagate to the following phases in the downscaled process which have great influence on the downscaled results. The higher accuracies of input products (including SSM, LST, NDVI and soil texture products) represent the better downscaled results. Moreover, different remotely

sensed SSM products would take various values for the same pixels and may have quite different accuracies. The accuracy of downscaled SSM highly depends on the accuracy of original AMSR-E data. In this experiment, the downscaling strategy has been realized on the LPRM AMSR-E product, which can be extended to other SSM products. For instance, SSM product of Climate Change Initiative from the European Space Agency will be attempted in our future work. The ground measurements are point observations and are insufficient to describe the spatial pattern of SSM. It is still needed to validate the spatial patterns of the downscaled SSM. However, this requires a spatially distributed reference dataset which are still not available. The precipitation might be an alternative dataset as an indirect reference.

The benefit from the point measurements is derived by their use to enhance the SSM estimations. We have undertaken preliminary experiments using an SVR model for calibration. The fitted SVR model can only be used under conditions similar to the ground stations, because the ground stations were concentrated within a limited area and not distributed uniformly throughout the entire region. In fact, additional features could be derived from the temporal variations of the in situ SSM measurements. Our future research efforts will be aimed at improving the downscaled SSM estimations by integrating additional characteristics of the temporal changes of SSM using time series analysis methods.

5. Conclusions

Downscaling offers the potential to transform coarse-resolution SSM observations to a finer resolution to support monitoring over large areas. To obtain temporally continuous SSM estimations under heterogeneous conditions, this study developed a downscaling methodology to overcome the full-coverage variable limitation of existing downscaling methods that use visible/infrared data as ancillary information. Under the proposed methodology, the GWATARK method is used to address local spatial heterogeneity, and multiscale ancillary variables are incorporated for better representation of the spatial pattern of SSM at different resolutions. For cloud-free days, the GWATARK-based

stepwise method is applied to downscale coarse-resolution SSM products by integrating multiscale ancillary data. Then, the downscaled results obtained for cloud-free days are used to generate fine-resolution SSM estimations for cloudy days by modeling the relationship with interpolated fine-resolution SSM data from another source. This method was demonstrated through application to the AMSR-E SSM products for ascending and descending overpasses of the TP, to produce temporally continuous 1-km-resolution SSM estimations for a six-month period. In comparison with the in situ measurements, the adopted statistical indices showed that the downscaled SSM estimations were reasonably accurate. The same comparison was also performed between the corresponding aggregated SSM values for two 25-km grid pixels to avoid scaling differences in the validation. Both qualitative and quantitative evaluations indicated the high potential of our proposed method for producing fine-resolution SSM images. However, the uncertainties associated with both the input variables and the models, which might have considerable effect on the accuracy of the downscaled SSM estimations, should be explored in future research. Despite the noted limitations, the proposed user-friendly methodology could be applied to other continuous parameters, and it could also be extended easily by the incorporation of additional multiscale ancillary covariates to attain temporally continuous series.

Acknowledgments

This work was supported by the National Natural Science Foundation for Distinguished Young Scholars of China (No. 41725006), and two Key Programs of the National Natural Science Foundation of China (No. 41531174 and No. 41531179). The authors would like to thank all the data producers.

References

- Ahmad, S., Kalra, A., Stephen, H., 2010. Estimating soil moisture using remote sensing data: a machine learning approach. *Adv. Water Resour.* 33 (1), 69–80. <http://dx.doi.org/10.1016/j.advwatres.2009.10.008>.
- Atkinson, P.M., 2013. Downscaling in remote sensing. *Int. J. Appl. Earth Obs. Geoinf.* 22 (1), 106–114. <http://dx.doi.org/10.1016/j.jag.2012.04.012>.
- Chakrabarti, S., Bongiovanni, T., Judge, J., et al., 2014. Assimilation of SMOS soil moisture for quantifying drought impacts on crop yield in agricultural regions. *IEEE J. Sel. Top. Appl. Earth Obs. Remote Sens.* 7 (9), 3867–3879. <http://dx.doi.org/10.1109/JSTARS.2014.2315999>.
- Chauhan, N.S., Miller, S., Ardanuy, P., 2003. Spaceborne soil moisture estimation at high resolution: a microwave-optical/IR synergistic approach. *Int. J. Remote Sens.* 24 (22), 4599–4622. <http://dx.doi.org/10.1080/0143116031000156837>.
- Chen, C.F., Valdez, M.C., Chang, N.B., et al., 2014. Monitoring spatiotemporal surface soil moisture variations during dry seasons in central America with multisensor cascade data fusion. *IEEE J. Sel. Top. Appl. Earth Obs. Remote Sens.* 7 (11), 4340–4355. <http://dx.doi.org/10.1109/JSTARS.2014.2347313>.
- Chen, B., Huang, B., Chen, L., Xu, B., 2016. Spatially and temporally weighted regression: a novel method to produce continuous cloud-free landsat imagery. *IEEE Trans. Geosci. Remote Sens.* 55 (1), 27–37. <http://dx.doi.org/10.1109/TGRS.2016.2580576>.
- Chen, W., Shen, H., Huang, C., Li, X., 2017. Improving soil moisture estimation with a dual ensemble kalman smoother by jointly assimilating AMSR-E brightness temperature and MODIS LST. *Remote Sens.* 9 (3), 273. <http://dx.doi.org/10.3390/rs9030273>.
- Colliander, A., Fisher, J.B., Halverson, G., et al., 2017. Spatial downscaling of SMAP soil moisture using MODIS land surface temperature and NDVI during SMAPVEX15. *IEEE Geosci. Remote Sens. Lett.* 1–5. <http://dx.doi.org/10.1109/LGRS.2017.2753203>.
- Cressie, N., 1988. Spatial prediction and ordinary kriging. *Math. Geol.* 20 (4), 405–421. <http://dx.doi.org/10.1007/BF00892986>.
- Das, N.N., Entekhabi, D., Njoku, E.G., 2011. An algorithm for merging smap radiometer and radar data for high-resolution soil-moisture retrieval. *IEEE Trans. Geosci. Remote Sens.* 49 (5), 1504–1512. <http://dx.doi.org/10.1109/TGRS.2010.2089526>.
- Dente, L., Vekerdy, Z., Wen, J., Su, Z., 2012. Magu network for validation of satellite-derived soil moisture products. *Int. J. Appl. Earth Obs. Geoinf.* 17, 55–65. <http://dx.doi.org/10.1016/j.jag.2011.11.004>.
- Djamaï, N., Magagi, R., Goïta, K., et al., 2016. A combination of DISPATCH downscaling algorithm with CLASS land surface scheme for soil moisture estimation at fine scale during cloudy days. *Remote Sens. Environ.* 184, 1–14. <http://dx.doi.org/10.1016/j.rse.2016.06.010>.
- Entekhabi, D., Njoku, E.G., Neill, P.E., et al., 2010. The soil moisture active passive (SMAP) mission. *Proc. IEEE* 98 (5), 704–716. <http://dx.doi.org/10.1109/JPROC.2010.2043918>.
- Ge, Y., Wang, J.H., Heuvelink, G.B.M., et al., 2015. Sampling design optimization of a wireless sensor network for monitoring ecohydrological processes in the Babao River basin, China. *Int. J. Geogr. Inf. Sci.* 29 (1), 92–110. <http://dx.doi.org/10.1080/13658816.2014.948446>.
- Harris, P., Fotheringham, A.S., Crespo, R., Charlton, M., 2010. Erratum to: the use of geographically weighted regression for spatial prediction: an evaluation of models using simulated data sets. *Math. Geosci.* 42 (6), 657–680. <http://dx.doi.org/10.1007/s11004-010-9284-7>.
- Hengl, T., de Jesus, J.M., MacMillan, R.A., et al., 2014. SoilGrids1km—global soil information based on automated mapping. *PLoS One* 9 (8), e105992. <http://dx.doi.org/10.1371/journal.pone.0114788>.
- Hengl, T., de Jesus, J.M., Heuvelink, G.B., et al., 2017. SoilGrids250m: global gridded soil information based on machine learning. *PLoS One* 12 (2), e0169748. <http://dx.doi.org/10.1371/journal.pone.0169748>.
- Jackson, T.J., Cosh, M.H., Bindlish, R., et al., 2010. Validation of advanced microwave scanning radiometer soil moisture products. *IEEE Trans. Geosci. Remote Sens.* 48 (12), 4256–4272. <http://dx.doi.org/10.1109/TGRS.2010.2051035>.
- Jarvis, A., Reuter, H.I., Nelson, A., Guevara, E., 2008. Hole-filled SRTM for the Globe Version 4. Available online: <http://srtm.csi.cgiar.org/>. (Accessed on 31 January 2016).
- Jensen, J.B., Høyer, S., Jensen, M.E., 2011. Soil moisture estimation through ASCAT and AMSR-E sensors: an intercomparison and validation study across Europe. *Remote Sens. Environ.* 115 (12), 3390–3408. <http://dx.doi.org/10.1016/j.rse.2011.08.003>.
- Jin, R., Li, X., Yan, B., et al., 2014. A nested ecohydrological wireless sensor network for capturing the surface heterogeneity in the midstream areas of the Heihe River Basin. *IEEE Geosci. Remote Sens. Lett.* 11 (11), 2015–2019. <http://dx.doi.org/10.1109/LGRS.2014.2319085>.
- Jin, Y., Ge, Y., Wang, J.H., et al., 2017. Downscaling AMSR-2 soil moisture data with geographically weighted area-to-area regression kriging. *IEEE Trans. Geosci. Remote Sens.* 1–15. <http://dx.doi.org/10.1109/TGRS.2017.2778420>. PP (99).
- Kaheil, Y.H., Gill, M.K., McKee, M., et al., 2008. Downscaling and assimilation of surface soil moisture using ground truth measurements. *IEEE Trans. Geosci. Remote Sens.* 46 (5), 1375–1384. <http://dx.doi.org/10.1109/TGRS.2008.916086>.
- Kang, J., Jin, R., Li, X., et al., 2017. High spatio-temporal resolution mapping of soil moisture by integrating wireless sensor network observations and MODIS apparent thermal inertia in the Babao River Basin, China. *Remote Sens. Environ.* 191, 232–245. <http://dx.doi.org/10.1016/j.rse.2017.01.027>.
- Kerr, Y.H., Waldteufel, P., Wigneron, J.P., et al., 2002. Soil moisture retrieval from space: the soil moisture and ocean salinity (SMOS) mission. *IEEE Trans. Geosci. Remote Sens.* 39 (8), 1729–1735. <http://dx.doi.org/10.1109/36.942551>.
- Koster, R.D., Mahanama, S.P.P., Yamada, T.J., et al., 2011. The second phase of the global land–atmosphere coupling experiment: soil moisture contributions to subseasonal forecast skill. *J. Hydrometeorol.* 12 (5), 805–822. <http://dx.doi.org/10.1175/2011JHM1365.1>.
- Leng, P., Song, X., Li, Z.L., Ma, J., et al., 2014. Bare surface soil moisture retrieval from the synergistic use of optical and thermal infrared data. *Int. J. Remote Sens.* 35 (3), 988–1003. <http://dx.doi.org/10.1080/01431161.2013.875237>.
- Leng, P., Song, X., Duan, S.B., Li, Z.L., 2016. A practical algorithm for estimating surface soil moisture using combined optical and thermal infrared data. *Int. J. Appl. Earth Obs. Geoinf.* 52 (52), 338–348. <http://dx.doi.org/10.1016/j.jag.2016.07.004>.
- Leng, P., Song, X., Duan, S., Li, Z., 2017. Generation of continuous surface soil moisture dataset using combined optical and thermal infrared images. *Hydrol. Processes* 31, 1398–1407. <http://dx.doi.org/10.1002/hyp.11113>.
- Li, X., Zhang, G., He, C., 2015. Watershed science: bridging new advances in hydrological science with good management of river basins. *Science China. Earth Sci.* 58 (1), 1. <http://dx.doi.org/10.1007/s11430-014-5037-7>.
- Likas, A., Vlassis, N., Verbeek, J.J., 2003. The global k – means clustering algorithm. *Pattern Recogn.* 36 (2), 451–461.
- Malbêteau, Y., Merlin, O., Gascoin, S., et al., 2017. Normalizing land surface temperature data for elevation and illumination effects in mountainous areas: a case study using ASTER data over a steep-sided valley in Morocco. *Remote Sens. Environ.* 189, 25–39. <http://dx.doi.org/10.1016/j.rse.2016.11.010>.
- Merlin, O., Escorihuela, M.J., Mayoral, M.A., et al., 2013. Self-calibrated evaporation-based disaggregation of SMOS soil moisture: an evaluation study at 3 km and 100 m resolution in Catalunya, Spain. *Remote Sens. Environ.* 130, 25–38. <http://dx.doi.org/10.1016/j.rse.2012.11.008>.
- Merlin, O., Malbêteau, Y., Notfi, Y., et al., 2015. Performance metrics for soil moisture downscaling methods: application to DISPATCH data in central Morocco. *Remote Sens.* 7, 3783–3807. <http://dx.doi.org/10.3390/rs70403783>.
- Naeimi, V., Scipal, K., Bartalis, Z., Hasenauer, S., Wagner, W., 2009. An improved soil moisture retrieval algorithm for ers and metop scatterometer observations. *IEEE Trans. Geosci. Remote Sens.* 47 (7), 1999–2013. <http://dx.doi.org/10.1109/TGRS.2008.2011617>.
- Njoku, E.G., Wilson, W.J., Yueh, S.H., Dinardo, S.J., 2002. Observations of soil moisture using a passive and active low-frequency microwave airborne sensor during sgp99. *IEEE Trans. Geosci. Remote Sens.* 40 (12), 2659–2673. <http://dx.doi.org/10.1109/TGRS.2002.807008>.
- Njoku, E.G., Jackson, T.J., Lakshmi, V., Chan, T.K., Nghiem, S.V., 2003. Soil moisture retrieval from AMSR-E. *IEEE Trans. Geosci. Remote Sens.* 41 (2), 215–229. <http://dx.doi.org/10.1109/TGRS.2002.808243>.
- Noborio, K., 2001. Measurement of soil water content and electrical conductivity by time domain reflectometry: a review. *Comput. Electron. Agric.* 31 (3), 213–237. [http://dx.doi.org/10.1016/S0168-1699\(00\)00184-8](http://dx.doi.org/10.1016/S0168-1699(00)00184-8).
- Ochsner, T.E., Cosh, M.H., Cuenca, R.H., et al., 2013. State of the art in large-scale soil moisture monitoring. *Soil Sci. Soc. Am. J.* 77 (6), 1888–1919. <http://dx.doi.org/10.1016/j.jag.2011.11.004>.

- 2136/sssaj2013.03.0093.
- Owe, M., Jeu, R.D., Holmes, T., 2008. Multisensor historical climatology of satellite-derived global land surface moisture. *J. Geophys. Res. Earth Surf.* 113 (F1), 196–199. <http://dx.doi.org/10.1029/2007JF000769>.
- Peng, J., Loew, A., Merlin, O., et al., 2017. A review of spatial downscaling of satellite remotely sensed soil moisture. *Rev. Geophys.* 55 (2), 341–366. <http://dx.doi.org/10.1002/2016RG000543>.
- Piles, M., Camps, A., Vall-Llossera, M., et al., 2011. Downscaling SMOS-derived soil moisture using MODIS visible/infrared data. *IEEE Trans. Geosci. Remote Sens.* 49 (9), 3156–3166. <http://dx.doi.org/10.1109/TGRS.2011.2120615>.
- Qin, J., Yang, K., Lu, N., Chen, Y., Zhao, L., Han, M., 2013. Spatial upscaling of in-situ soil moisture measurements based on MODIS-derived apparent thermal inertia. *Remote Sens. Environ.* 138, 1–9. <http://dx.doi.org/10.1016/j.rse.2013.07.003>.
- Rakwatin, P., Takeuchi, W., Yasuoka, Y., 2009. Restoration of Aqua MODIS band 6 using histogram matching and local least squares fitting. *IEEE Trans. Geosci. Remote Sens.* 47 (2), 613–627. <http://dx.doi.org/10.1109/TGRS.2008.2003436>.
- Ray, R.L., Jacobs, J.M., Cosh, M.H., 2010. Landslide susceptibility mapping using downscaled AMSR-E soil moisture: a case study from Cleveland Corral, California, US. *Remote Sens. Environ.* 114 (11), 2624–2636. <http://dx.doi.org/10.1016/j.rse.2010.05.033>.
- Reichle, R.H., Entekhabi, D., Mclaughlin, D.B., 2010. Downscaling of radio brightness measurements for soil moisture estimation: a four-dimensional variational data assimilation approach. *Water Resour. Res.* 37 (9), 2353–2364. <http://dx.doi.org/10.1029/2001WR000475>.
- Robock, A., Vinnikov, K.Y., Srinivasan, G., et al., 2000. The global soil moisture data bank. *Bull. Am. Meteorol. Soc.* 81 (6), 1281–1299. <http://dx.doi.org/10.1175/1520-0477>.
- Roy, D.P., Ju, J., Lewis, P., et al., 2008. Multi-temporal modis-landsat data fusion for relative radiometric normalization, gap filling, and prediction of landsat data. *Remote Sens. Environ.* 112 (6), 3112–3130. <http://dx.doi.org/10.1016/j.rse.2008.03.009>.
- Sahoo, A.K., Lannoy, G.J.M.D., Reichle, R.H., Houser, P.R., 2013a. Assimilation and downscaling of satellite observed soil moisture over the little river experimental watershed in Georgia, USA. *Adv. Water Resour.* 52 (2), 19–33. <http://dx.doi.org/10.1016/j.advwatres.2012.08.007>.
- Sahoo, A.K., Lannoy, G.J.M.D., Reichle, R.H., Houser, P.R., 2013b. Assimilation and downscaling of satellite observed soil moisture over the little river experimental watershed in Georgia, USA. *Adv. Water Resour.* 52 (2), 19–33. <http://dx.doi.org/10.1016/j.advwatres.2012.08.007>.
- Samouëlian, A., Cousin, I., Tabbagh, A., Bruand, A., Richard, G., 2005. Electrical resistivity survey in soil science: a review. *Soil Tillage Res.* 83 (2), 173–193. <http://dx.doi.org/10.1016/j.still.2004.10.004>.
- Seneviratne, S.I., Corti, T., Davin, E.L., et al., 2010. Investigating soil moisture-climate interactions in a changing climate: a review. *Earth Sci. Rev.* 99 (3–4), 125–161. <http://dx.doi.org/10.1016/j.earscirev.2010.02.004>.
- Srivastava, P.K., Han, D., Ramirez, M.R., Islam, T., 2013. Machine learning techniques for downscaling SMOS satellite soil moisture using MODIS land surface temperature for hydrological application. *Water Resour. Manage.* 27 (8), 3127–3144. <http://dx.doi.org/10.1007/s11269-013-0337-9>.
- Su, Z., Wen, J., Dente, L., et al., 2011. The Tibetan Plateau observatory of plateau scale soil moisture and soil temperature (Tibet-Obs) for quantifying uncertainties in coarse resolution satellite and model products. *Hydrol. Earth Syst. Sci.* 15 (7), 2303–2316. <http://dx.doi.org/10.5194/hess-15-2303-2011>.
- Team, R.D.C., 2014. R: a language and environment for statistical computing. *Computing* 14, 12–21. Available from: <https://www.r-project.org/>.
- Thattai, D., Islam, S., 2000. Spatial analysis of remotely sensed soil moisture data. *J. Hydrol. Eng.* 5 (4), 386–392. [http://dx.doi.org/10.1061/\(ASCE\)1084-0699\(2000\)5:4\(386\)](http://dx.doi.org/10.1061/(ASCE)1084-0699(2000)5:4(386)).
- Tubiello, F.N., Rosenzweig, C., Goldberg, R.A., et al., 2002. Effects of climate change on US crop production: simulation results using two different GCM scenarios. Part I: wheat, potato, maize, and citrus. *Clim. Res.* 20 (3), 259–270. <http://dx.doi.org/10.3354/cr020259>.
- Vapnik, V.N., 2000. *The Nature of Statistical Learning Theory*, second. Springer, New York. <http://dx.doi.org/10.1007/978-1-4757-3264-1>.
- Wagner, W., Pathe, C., Doubkova, M., et al., 2008. Temporal stability of soil moisture and radar backscatter observed by the Advanced Synthetic Aperture Radar (ASAR). *Sensors* 8 (2), 1174–1197. <http://dx.doi.org/10.3390/s80201174>.
- Wilson, D.J., Western, A.W., Grayson, R.B., 2005. A terrain and data-based method for generating the spatial distribution of soil moisture. *Adv. Water Resour.* 28 (1), 43–54. <http://dx.doi.org/10.1016/j.advwatres.2004.09.007>.
- Yang, K., Watanabe, T., Koike, T., et al., 2007. Auto-calibration system developed to assimilate AMSR-E data into a land surface model for estimating soil moisture and the surface energy budget. *J. Meteorol. Soc. Jpn.* 85A, 229–242. <http://dx.doi.org/10.2151/jmsj.85A.229>.
- Yang, K., Qin, J., Zhao, L., et al., 2013. A multiscale soil moisture and freeze-thaw monitoring network on the third pole. *Bull. Am. Meteorol. Soc.* 94 (12), 1907–1916. <http://dx.doi.org/10.1175/BAMS-D-12-00203.1>.
- Yang, K., Zhu, L., Chen, Y., et al., 2016. Land surface model calibration through microwave data assimilation for improving soil moisture simulations. *J. Hydrol.* 533, 266–276. <http://dx.doi.org/10.1016/j.jhydrol.2015.12.018>.
- Zeng, J., Li, Z., Chen, Q., et al., 2015. Evaluation of remotely sensed and reanalysis soil moisture products over the Tibetan Plateau using in-situ observations. *Remote Sens. Environ.* 163, 91–110. <http://dx.doi.org/10.1016/j.rse.2015.03.008>.
- Zhan, X., Houser, P.R., Walker, J.P., Crow, W.T., 2006. A method for retrieving high-resolution surface soil moisture from hydros l-band radiometer and radar observations. *IEEE Trans. Geosci. Remote Sens.* 44 (6), 1534–1544. <http://dx.doi.org/10.1109/TGRS.2005.863319>.
- Zhao, W., Li, Z.L., Wu, H., Tang, B.H., et al., 2013. Determination of bare surface soil moisture from combined temporal evolution of land surface temperature and net surface shortwave radiation. *Hydrol. Processes* 27 (19), 2825–2833. <http://dx.doi.org/10.1002/hyp.9410>.
- Zreda, M., Shuttleworth, W.J., Zeng, X., et al., 2012. COSMOS: the cosmic-ray soil moisture observing system. *Hydrol. Earth Syst. Sci.* 16 (11), 4079–4099. <http://dx.doi.org/10.5194/hess-16-4079-2012>.